J. Fluid Mech. (2024), *vol*. 985, A37, doi:10.1017/jfm.2024.254

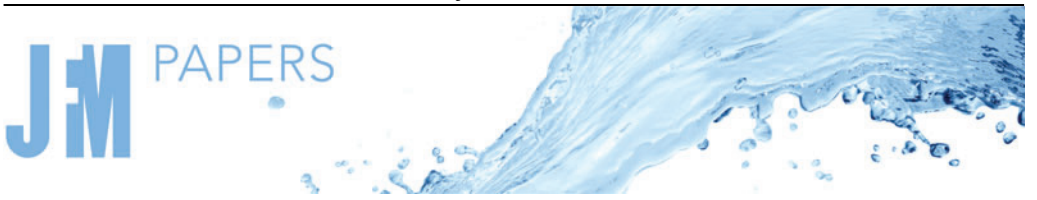

Elasto-inertial instability in torsional flows of shear-thinning viscoelastic fluids

Rishabh V. More[1], **R. Patterson**[2], **E. Pashkovski**[2] **and G.H. McKinley**[1],†

[1]Department of Mechanical Engineering, Massachusetts Institute of Technology, Cambridge, MA 02139, USA

[2]The Lubrizol Corporation, 29400 Lakeland Blvd., Wickliffe, OH 44092, USA

(Received 17 October 2023; revised 15 February 2024; accepted 26 February 2024)

It is well known that inertia-free shearing flows of a viscoelastic fluid with curved streamlines, such as the torsional flow between a rotating cone and plate or the flow in a Taylor–Couette geometry, can become unstable to a three-dimensional time-dependent instability at conditions exceeding a critical Weissenberg (*Wi*) number. However, the combined effects of fluid elasticity, shear thinning and finite inertia (as quantified by the Reynolds number *Re*) on the onset of elasto-inertial instabilities are not fully understood. Using a set of cone–plate geometries, we experimentally explore the entire *Wi*–*Re* phase space for a series of nonlinear viscoelastic fluids (with the dependence on shear rate $\dot{\gamma}$ quantified using a shear-thinning parameter $\beta_P(\dot{\gamma})$). We tune $\beta_P(\dot{\gamma})$ by varying the dissolved polymer concentration in solution. This progressively reduces shear thinning but leads to finite inertial effects before the onset of elastic instability, and thus naturally results in elasto-inertial coupling. Time-resolved rheometric measurements and flow visualization experiments allow us to investigate the effects of flow geometry, and document the combined effects of varying *Wi*, *Re* and $\beta_P(\dot{\gamma})$ on the emergence of secondary motions at the onset of instability. The resulting critical state diagram quantitatively depicts the competition between the stabilizing effects of shear thinning and the destabilizing effects of inertia. We extend the curved streamline instability criterion of Pakdel & McKinley (*Phys. Rev. Lett.*, vol. 77, no. 12, 1996, p. 2459) for the onset of purely elastic instability in curvilinear geometries by using scaling arguments to incorporate shear thinning and finite inertial effects. The augmented condition facilitates predictions of the onset of instability over a broader range of flow conditions, and thus bridges the gap between purely elastic and elasto-inertial curved streamline instabilities.

Key words: viscoelasticity, polymers, nonlinear instability

† Email address for correspondence: gareth@MIT.EDU

1. Introduction

Rotational flows with curvilinear streamlines are routinely encountered in many applications, such as transport and handling of fluids, dispensing, spin coating, flows in centrifuges, extruders, flows around objects, lubrication and journal bearing flows, polymer processing, as well as rheometry. The torsional flow between co-axial parallel disks or between a cone and a plate are canonical examples in which a unidirectional shear flow with curved streamlines is generated; hence, they are commonly employed in rheometry and as canonical systems in which to study viscoelastic flow stability. Even in the limit of small cone angles, steady secondary motions and flow instabilities can develop (Larson 1992; Shaqfeh 1996) owing to nonlinearities stemming from interactions among streamline curvature, fluid inertia and non-Newtonian fluid properties.

Specifically, in a cone-and-plate geometry with cone radius R, a cone angle θ and rotating at speed Ω, a Newtonian fluid with a constant viscosity η_s and density ρ experiences the onset of inertially driven toroidal secondary motions beyond a critical rotation rate (Olagunju 1997), and at higher rates, inertial turbulence, when the centrifugal force becomes dominantly larger than the viscous force (Sdougos, Bussolari & Dewey 1984). However, highly elastic 'Boger fluids' with a constant viscosity η_0 exhibit a time-dependent transition to an unstable state characterized by an enhanced and fluctuating shear stress (initially interpreted as anti-thixotropic behaviour: Jackson, Walters & Williams 1984), when sheared beyond a critical value of the dimensionless rotational speed, or Deborah number $De = \tau_s\Omega$, where τ_s is the shear relaxation time (McKinley *et al.* 1991), which is constant for a Boger fluid. The unstable flow manifests as radially propagating logarithmic spiral vortices (Öztekin, Brown & McKinley 1994). Furthermore, linear stability analysis of the cone-and-plate flow using different constitutive models reveals the critical role of the dimensionless geometry parameter $1/\theta$ (Olagunju 1997) on the onset of elastic instabilities, and this sensitivity has also been confirmed by experiments (Öztekin *et al.* 1994; McKinley *et al.* 1995). Thus, the instability is a function of both the dimensionless rotational speed, i.e. $De = \tau_s\Omega$, and a dimensionless form of the shear rate $\dot{\gamma} = \Omega/\theta$, i.e. the Weissenberg number $Wi = \tau_s\dot{\gamma}$. A comparison of critical conditions in the *Wi*–*De* state diagram with linear stability results indeed validates this codependency (Öztekin *et al.* 1994; McKinley *et al.* 1995). Thorough reviews of these earlier studies of viscometric flow instabilities can be found from Larson (1992) and Shaqfeh (1996).

Pakdel & McKinley (1996) argued that this type of instability generically arises due to the non-uniform stretching of the polymer molecules in a curvilinear shearing flow, which amplifies the elastic 'hoop stress' in the fluid. This enters the radial momentum balance and amplifies radial velocity perturbations, making the torsional flow of viscoelastic fluids unstable under sufficiently strong driving conditions. They proposed an instability criterion in terms of the product of *Wi* and *De* exceeding a critical magnitude denoted M_c, and showed that this could be written in the generic form $DeWi = (\tau_s\Omega)(\tau_s\dot{\gamma}) > M_c^2$. More generally, we can write $De = \tau_s U/\mathcal{R}$, with $\mathcal{R}$ being the (geometry-dependent) characteristic radius of the streamline curvature and U being the characteristic streamwise fluid velocity. The ratio $\mathcal{R}/U$ gives the characteristic convective time of a flow experiment. Thus, to take into account, more generally, the curvature of a two-dimensional flow and the action of tensile stress difference along the streamlines, this criterion for the onset of instability can be rewritten as (McKinley, Pakdel & Öztekin 1996)

$$DeWi = \frac{\tau_s U}{\mathcal{R}}\frac{N_1}{\sigma} \geq M_c^2, \tag{1.1}$$

where U is a characteristic streamwise fluid velocity, $\mathcal{R}$ is the geometry-dependent characteristic radius of curvature of the streamline, N_1 is the first normal stress difference in the fluid and $\sigma = \eta_0\dot{\gamma}$ is the shear stress. Furthermore, linear stability analysis of the steady base flow of an Oldroyd-B fluid in a cone-and-plate geometry (Olagunju & Cook 1993; Olagunju 1995, 1997), as well as in a Taylor–Couette geometry (Schaefer, Morozov & Wagner 2018), shows that the viscosity ratio parameter $\beta_P = \eta_P/\eta_0$ (where η_P is the polymer contribution to the fluid viscosity and η_∞ is the Newtonian plateau viscosity at high shear rates, such that $\eta_0 = \eta_P + \eta_\infty$) significantly affects the nature of the elastic instability. The effect of β_P can be readily incorporated in the condition for purely elastic instability ((1.1)) by substituting the Oldroyd-B result $N_1 = 2\eta_P\tau_s\dot{\gamma}^2$ and $\sigma = (\eta_P + \eta_\infty)\dot{\gamma}$, which gives

$$\frac{\tau_s U}{\mathcal{R}}\frac{2\eta_P\tau_s\dot{\gamma}}{\eta_0} = \frac{\tau_s U}{\mathcal{R}}2\beta_P\tau_s\dot{\gamma} \geq M_c^2 \implies DeWi \geq \frac{M_c^2}{2\beta_P}. \tag{1.2}$$

In dilute polymer solutions, as $\beta_P \to 0$, the critical shear rate $\dot{\gamma}_c = \Omega_c/\theta$ required for the onset of instability diverges, in accordance with experiments. More recently, Schiamberg *et al.* (2006) have studied the effect of changing the viscosity ratio β_P on the onset of secondary motion and the evolution towards a fully developed nonlinear state commonly referred to as 'elastic turbulence' in a parallel plate geometry using a polyacrylamide Boger fluid.

Theoretically, it should be possible to modify the criterion in (1.1) for the onset of purely elastic instability in shear-thinning viscoelastic fluids by allowing τ_s and η_P to both be shear-rate dependent and writing them as functions of the applied shear rate $\dot{\gamma}$. However, the reduction in the viscosity due to shear thinning means a concomitant increase in inertial effects, which can systematically modify the purely elastic instabilities observed in Boger fluids at very low Reynolds numbers, $Re \ll 1$. This inherent nonlinear coupling between inertia and elasticity in shear-thinning viscoelastic fluids makes the corresponding torsional flows more challenging to understand, especially the critical conditions for the onset of elasto-inertial instabilities. Hence, there have been relatively few studies elucidating the effect of shear thinning on viscoelastic flow stability. Dutcher & Muller (2013), Schaefer *et al.* (2018) and Lacassagne, Cagney & Balabani (2021) have investigated shear-thinning-mediated elasto-inertial transitional pathways in Taylor–Couette geometries. Similar observations have also been made in the case of the flow of a shear-thinning viscoelastic fluid through a tube (Chandra *et al.* 2019). Each of these studies reveals the inherent coupling of fluid elasticity (which tends to destabilize the base shearing flow) and inertia (which tends to restabilize the unsteady flow of viscoelastic fluids). The resulting stability diagrams are best represented by three-dimensional plots in terms of dimensionless parameters characterizing the geometry, fluid elasticity and the inertia of the flow (Dutcher & Muller 2009).

Very recently, Datta *et al.* (2022) reviewed our current understanding of the broader topic of viscoelastic flow instabilities and elastic turbulence. They suggest representing the critical conditions for the onset of viscoelastic flow instabilities in the *Wi–Re* plane. In this plane, a set of exploratory experiments with a given rate-independent viscoelastic fluid in a fixed geometry trace a line with a slope given by the elasticity number $El = Wi/Re$ (see figure 4 of Datta *et al.* 2022) eventually intersecting with a corresponding stability boundary demarcating the critical conditions for the onset of instability. Tracing the critical conditions using different viscoelastic fluids and flow geometries enables exploration of the entire phase space, and the various flow states observed will showcase the transitions in the instability mechanisms as inertial, elastic and geometric effects are varied. In the

c_P (wt.%)	ρ (kg m^{-3})	Γ (mN m^{-1})	η_s (Pa s)	$[\eta]$ (dL g^{-1})	c^* (wt.%)
0.30–3.00	873.1	29.7	0.018	3.69	0.23

Table 1. PIB polymer solution properties.

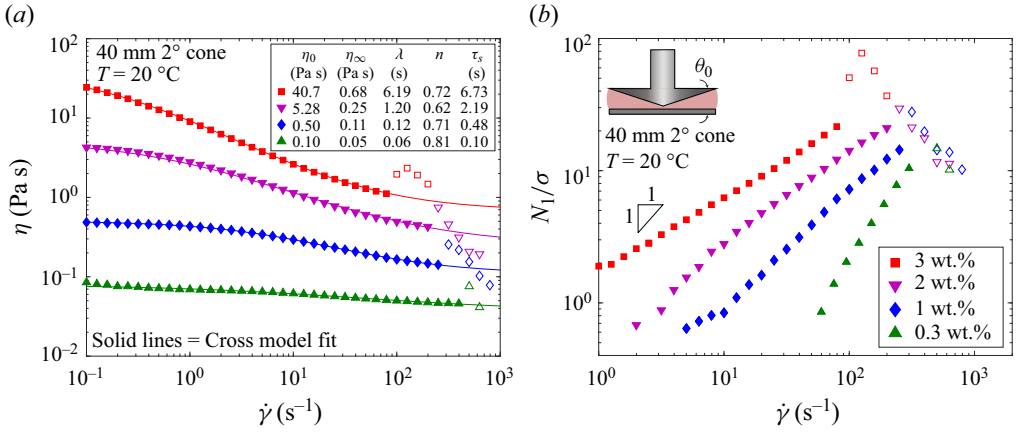

Figure 1. (*a*) Flow curve and (*b*) rate-dependent stress ratio $S_R = N_1(\dot{\gamma})/\sigma(\dot{\gamma})$ of viscoelastic fluids used in this study. The viscometric properties of the PIB solutions (filled symbols) show a strong shear-thinning behaviour, which can be modelled with the Cross model (solid lines in panel *a*) before the onset of instability with best-fit parameters presented in the inset of panel (*a*). The sudden jump in the viscosity and stress ratio values above a certain critical shear rate (hollow symbols) occurs due to the onset of time-dependent flow instabilities arising from a combination of elasticity and inertia.

present work, we investigate the development of time-dependent instabilities in a family of shear-thinning viscoelastic polyisobutylene (PIB) solutions of different PIB concentrations (c_P) using a set of cone-and-plate geometries of different cone angles (θ) and radii (R) to elucidate the combined effects of fluid elasticity, shear thinning, inertia and geometry on the onset of torsional viscoelastic flow instabilities.

2. Materials and methods

We use polymeric solutions of PIB (MW $\approx 10^6$ g mol^{-1}) dissolved in a paraffinic oil (GADDTAC, Lubrizol Inc.). We perform all our measurements at a constant temperature $T = 20\,^{\circ}$C. The Newtonian base oil has a solvent viscosity $\eta_s = 18.07$ mPa s at $20\,^{\circ}$C. Dilute solution viscometry determines the polymer intrinsic viscosity to be $[\eta] = 3.69$ dL g^{-1} and this gives the critical overlap concentration of the polymer solute as $c^* \simeq 0.77/[\eta] = 0.23$ wt.% (Graessley 1980). The solutions were all measured to have a constant density $\rho = 873.1$ kg m^{-3} and surface tension $\Gamma = 29.7$ mN m^{-1}. We vary the dissolved concentration of polymer in the solution to change the viscoelastic properties. We work with three semi-dilute ($c_P > c^*$) solutions: 3 wt.%, 2 wt.% and 1 wt.%, respectively, and one close to c^* with $c_p = 0.3$ wt.%. In table 1, we summarize the key material properties for the family of polymeric fluids used in the study. These polymeric solutions are all shear thinning to various extents, with their viscoelasticity decreasing at lower concentrations, as shown in figure 1 and table 2.

c_P (wt.%)	η_0 (Pa s)	η_∞ (Pa s)	λ (s)	n
3.0	40.7	0.68	6.19	0.72
2.0	5.28	0.25	1.20	0.62
1.0	0.50	0.11	0.12	0.71
0.3	0.10	0.05	0.06	0.81

Table 2. Best fit parameters for the inelastic Cross model for the stable, steady-state rate-dependent shear viscosity data (figure 1*a*) of various PIB solutions used in this study.

The inelastic Cross model, $\eta(\dot{\gamma}) = \eta_\infty + (\eta_0 - \eta_\infty)/[1 + (\lambda\dot{\gamma})^n]$, does an excellent job at describing the viscosity as a function of shear rate for all solutions (for best-fit parameter values, see figure 1*a* and table 2). Here, η_0 and η_∞ are viscosities in the limit of zero and infinite shear rate, respectively, λ^{-1} is a measure of the characteristic shear rate for the onset of shear thinning, and n is the shear-thinning index. The extent of shear thinning in these viscoelastic solutions can be quantified in several ways. One direct metric is the ratio $\eta(\dot{\gamma})/\eta_0$. A more useful ratio that also provides consistency with earlier analysis, as we show later, is the dimensionless function $\beta_P(\dot{\gamma}) \equiv \eta_P(\dot{\gamma})/\eta(\dot{\gamma}) = [\eta(\dot{\gamma}) - \eta_\infty]/\eta(\dot{\gamma})$, which quantifies the relative polymer contribution to the total (rate-dependent) solution viscosity at a given shear rate.

Shear-thinning rheology also means that the first normal stress coefficient $\Psi_1 = N_1/\dot{\gamma}^2$ and the relaxation time of the solutions are no longer material constants, but become rate-dependent functions denoted by $\Psi_1(\dot{\gamma})$ and $\tau_s(\dot{\gamma})$. From the functional form of the upper-convected derivative, the first normal stress difference can be related to the shear stress and the relaxation time of the fluid through the expression $N_1(\dot{\gamma}) \simeq 2\tau_s\dot{\gamma}\sigma$ (Bird, Armstrong & Hassager 1987), which, after a slight rearrangement, gives $N_1(\dot{\gamma})/\sigma(\dot{\gamma}) \simeq 2\tau_s\dot{\gamma}$. This ratio of the first normal stress difference (N_1) to the shear stress in the sheared fluid (σ) is termed the stress ratio S_R and is a direct quantitative measure of nonlinear viscoelastic effects in these polymeric solutions (see figure 1*b*). The importance of nonlinear elastic effects at the onset of flow instability in each fluid is evident as the stress ratio $S_R = N_1/\sigma \gtrsim 10$. One can also eliminate $\dot{\gamma}$ by substituting $\dot{\gamma} = \sigma/\eta$ in the expression above, which gives $N_1 \approx 2(\tau_s/\eta)\sigma^2$. So, one can anticipate on theoretical grounds that N_1 will vary quadratically with σ. The quadratic dependence of the first normal stress difference N_1 on the shear stress is well known for polymer solutions (Lodge, Al-Hadithi & Walters 1987; Binding, Jones & Walters 1990) and has recently been documented in viscoelastic emulsions as well (Kibbelaar *et al.* 2023). This key observation that $N_1 \sim \sigma^2$ will be crucial later in enabling us to incorporate shear-thinning rheology effects in a unified critical instability criterion (cf. § 3.4).

Furthermore, in semi-dilute polymer solutions, τ_s and η are both typically power law functions of the polymer concentration c_P (Heo & Larson 2005). As a result, the modulus $G_c(c_P) \approx \eta(c_P)/\tau_s(c_P)$ only increases weakly with increasing the polymer concentration c_P. Hence, $N_1 \approx 2(\tau_s/\eta)\sigma^2 \approx \sigma^2/G_c(c_P)$ may be expected to only decrease weakly with the polymer concentration c_P in the fluids used. We plot the first normal stress difference N_1 as a function of the shear stress σ in figure 2 to test this prediction. We find that not only $N_1 \sim \sigma^2$, but this relationship also holds irrespective of the polymer concentration except when the flow becomes unsteady (hollow symbols). Thus, we can estimate the steady-state values of $N_1(\dot{\gamma})$ from measurements of steady-state shear stress alone as

$$N_1(\dot{\gamma}) = A\sigma(\dot{\gamma})^2, \tag{2.1}$$

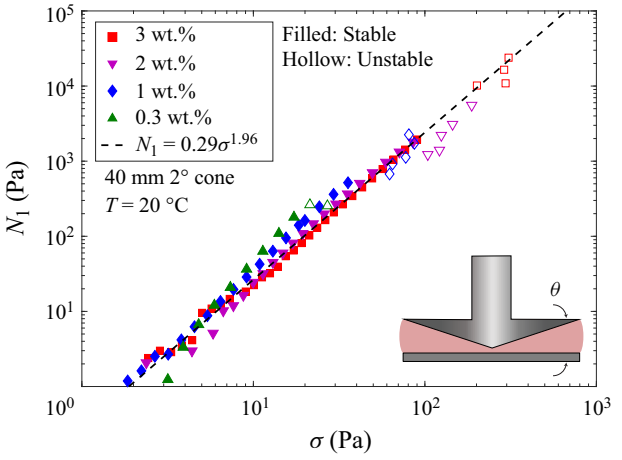

Figure 2. First normal stress difference N_1 plotted as a function of the shear stress σ in a 40 mm 2° geometry for all the PIB solutions used in this study. The data lie almost on a single curve irrespective of the polymer concentration in solution with a power-law best fit given by $N_1 \sim \sigma^{1.96}$, which is very close to the ideal quadratic dependence of N_1 with σ expected theoretically.

where A is a constant coefficient obtained from the rheological measurements shown in figure 2. For the fluids used in this study, we find $A = 0.29\ \text{Pa}^{-1}$.

To incorporate rate-dependent rheological effects in the criterion for the onset of elastic instabilities (cf. (1.1)), we use the more general definition of the Weissenberg number $Wi = N_1/2\sigma$ (White 1964), which can be simplified using (2.1) as

$$Wi \equiv \frac{N_1(\dot\gamma)}{2\sigma(\dot\gamma)} = \frac{A}{2}\sigma(\dot\gamma). \tag{2.2}$$

Shear-thinning rheology also results in a rate-dependent characteristic shear relaxation time $\tau_s(\dot\gamma)$, which enters (1.1). This relaxation time can be directly evaluated from experimental measurements of the first normal stress difference and the polymer contribution to the shear stress $\sigma_P = \eta_P(\dot\gamma)\dot\gamma$. We can thus define $\tau_s(\dot\gamma) = N_1(\dot\gamma)/(2\eta_P(\dot\gamma)\dot\gamma^2)$. After a slight rearrangement along with substituting $\sigma = \eta(\dot\gamma)\dot\gamma$ and $\beta_P(\dot\gamma) = \eta_P(\dot\gamma)/\eta(\dot\gamma)$, we can thus write

$$\tau_s(\dot\gamma) \equiv \frac{N_1(\dot\gamma)}{2\eta_P(\dot\gamma)\dot\gamma^2} = \frac{1}{\beta_P(\dot\gamma)\dot\gamma}\frac{N_1(\dot\gamma)}{2\sigma(\dot\gamma)}. \tag{2.3}$$

This general expression for the rate-dependent characteristic relaxation time of a viscoelastic fluid can be combined with (2.1) if it is validated experimentally for a given material system. For completeness, we note that this definition correctly reduces to the expression used in the literature (derived from the Oldroyd-B formulation) for the case of a non-shear-thinning Boger fluid; $N_1 = 2\tau_s\sigma_P\dot\gamma = 2\tau_s\eta_P\dot\gamma^2$, where $\eta_P = \eta_0 - \eta_s$, $\lim_{\dot\gamma\to 0}\Psi_1 = \Psi_{1,0} = 2\tau_s\eta_P$ and $\lim_{\dot\gamma\to 0}\tau_s(\dot\gamma) = \tau_s$. The rate-dependent shear relaxation time $\tau_s(\dot\gamma)$ defined in (2.3) can also be used (if desired) to define a rate-dependent Deborah number $De = \tau_s(\dot\gamma)\Omega$, which incorporates shear thinning in the relaxation time. In addition, the normal stress difference ratio $\psi = -\Psi_{2,0}/\Psi_{1,0}$ for the PIB solutions used in this study fall in the range 0.205–0.243 as measured from rod-climbing rheometry (More *et al.* 2023). Here, $\lim_{\dot\gamma\to 0}\Psi_2 = \Psi_{2,0}$ with Ψ_2 being the second normal stress coefficient. We have included additional rheological characterization

of the various PIB solutions used in this study, including small amplitude oscillatory shear measurements, in the supplementary material available at https://doi.org/10.1017/jfm.2024.254.

3. Results and discussion

As shown in figure 1(*a*), a sudden jump in the measured apparent *steady-state* shear viscosity is observed for all solutions beyond a sufficiently high shear rate when sheared in a cone-and-plate geometry. These measurements are not erroneous but are manifestations of the onset of time-dependent secondary motion beyond a critical (composition and geometry dependent) shear rate $\dot{\gamma}_c$. As a result, the stresses in the samples also suddenly increase due to large velocity disturbances. This is the origin of the so-called 'anti-thixotropic' transition (Jackson *et al.* 1984), observed and analysed previously for constant viscosity PIB Boger fluids (McKinley *et al.* 1991; Öztekin *et al.* 1994; Schiamberg *et al.* 2006). In the present study, we analyse the same instability for viscoelastic fluids with pronounced shear thinning, which inherently drives a transition of the instability mechanism from purely elastic to elasto-inertial as we gradually decrease the polymer concentration. Finally, we use the following conventions for the governing rate-dependent dimensionless parameters: (1) a subscript $_0$ denotes dimensionless parameters determined using material function values in the zero-shear-rate limit, i.e. without incorporating rate-dependent viscosity effects, e.g. $Re_0 = \rho\Omega R^2/\eta_0$, $Wi_0 = \tau_s\dot{\gamma}$; (2) the absence of any subscript denotes dimensionless parameters determined with the incorporation of rate-dependent viscosity effects, e.g. $Re = \rho\Omega R^2/\eta(\dot{\gamma})$, $Wi = \tau_s(\dot{\gamma})\dot{\gamma}$; and (3) a subscript $_c$ denotes the critical condition $\dot{\gamma} \to \dot{\gamma}_c$, e.g. $Re_c = \rho\Omega_c R^2/\eta(\dot{\gamma}_c)$, $Wi_c = \tau_s(\dot{\gamma}_c)\dot{\gamma}_c$.

3.1. *Time-dependent instability, power spectra and unsteady flow visualization*

The experimentally measured time-evolving shear stress $\sigma(t, \dot{\gamma})$ and first normal stress difference $N_1(t, \dot{\gamma})$ for a constant shear rate experiment in a 40 mm 2° cone-and-plate geometry are shown in figure 3 for two different PIB fluids. The transient responses of $\sigma(t)$ and $N_1(t)$ are typical of viscoelastic fluids; at short times, a rapid stress increase with an overshoot (and initial quadratic growth in N_1) is observed. At longer times, constant steady-state values are observed only when the imposed shear rate is less than a critical value $\dot{\gamma}_c$. Beyond this point, both $\sigma(t, \dot{\gamma})$ and $N_1(t, \dot{\gamma})$ increase rapidly to a new fluctuating state similar to the earlier observations for Boger fluids (McKinley *et al.* 1991). Calculations of the apparent viscosity and first normal stress difference from averaging these enhanced time-dependent measurements result in the sudden jump observed in figure 1. However, the time dependence of the unstable flow of the shear-thinning viscoelastic fluid has notable differences compared with a Boger fluid.

As we reduce the PIB concentration, the viscosity of the solutions decreases and inertial effects become increasingly important. The competition between the effects of shear thinning and the effects of inertia results in the onset of instability at a lower Wi_c than the elastic shear-thinning case of the 3 wt.% PIB solution. In addition, we observe a gradual decay in the mean amplitude of the stress fluctuations for the less concentrated PIB fluids due to slow irreversible sample ejection from the geometry edge as well as possible viscous heating effects (Calado, White & Muller 2005). As a result, the eventual steady-state value reached after the fluctuations in the $\sigma(t)$ and $N_1(t)$ response die out can be lower than the quasi-steady-state value achieved after the initial transient is completed (at times $t \sim O(10)s$). Thus, reducing the PIB concentration gradually shifts the instability mechanism from purely elastic to elasto-inertial, and shear thinning plays a

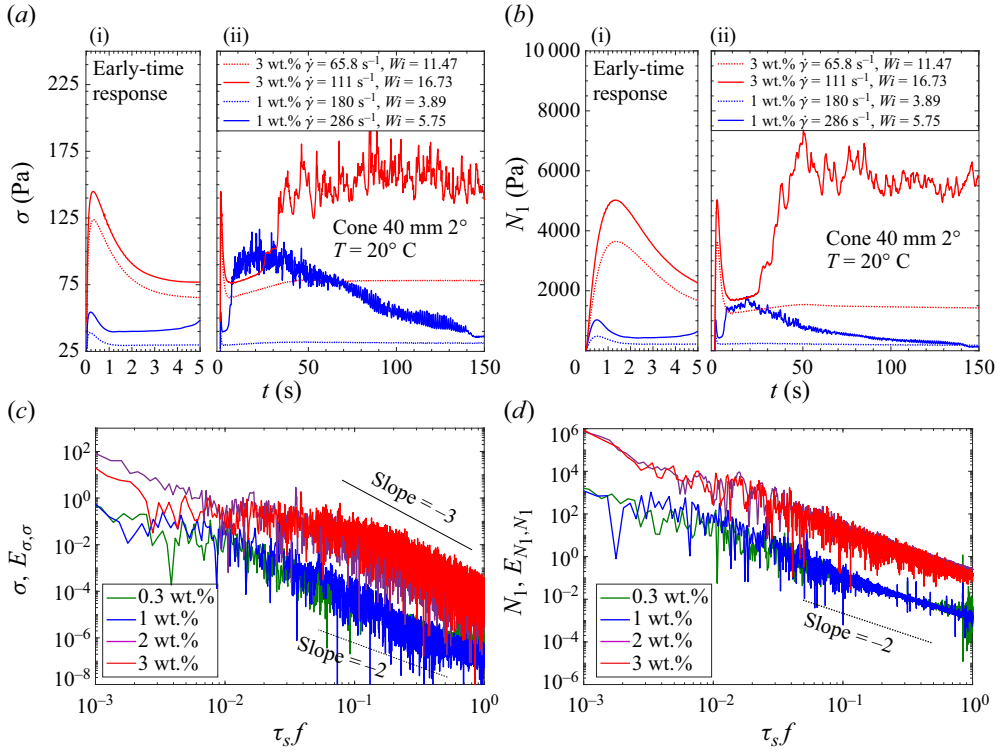

Figure 3. Time-dependent evolution in (*a*) shear stress and (*b*) the first normal stress difference of the 3 wt.% ($Re \lessapprox 1$) and the 1 wt.% ($Re \gtrapprox 10$) samples in a peak hold experiment at shear rates below (dotted lines) and above (solid lines) the critical shear rate for the onset of instability. The corresponding values of $Wi = N_1/2\sigma = A\sigma/2$ are also given. Power spectra for (*c*) shear stress and (*d*) the first normal stress difference N_1 for the unstable flows shown in panels (*a*) and (*b*) are shown as a function of dimensionless frequency $\tau_s f$, and all four different polymer concentrations probed in this study.

crucial role in determining the critical conditions for the onset of instability. This transition in the instability mechanism becomes clear from the power spectra of the shear stress σ (denoted $E_{\sigma\sigma}$) and the first normal stress difference N_1 (denoted $E_{N_1N_1}$) obtained by taking Fourier transforms of $\sigma(t)$ and $N_1(t)$ after the onset of time-dependent fluctuations. The corresponding power spectra for the fluid response (at $\dot{\gamma} > \dot{\gamma}_c$) are presented in figures 3(*c*) and 3(*d*), respectively. The slope of the power spectra progressively changes from -3 to -2 for $E_{\sigma\sigma}$ but remains unchanged for $E_{N_1N_1}$ as we gradually reduce the PIB concentration below 3 wt.%. Furthermore, when plotted as a function of an appropriate dimensionless frequency $\tau_s(\dot{\gamma})f$, the measured spectra fall onto two distinct curves: one for the more concentrated solutions (3 and 2 wt.%) and a separate curve for the less concentrated solutions (1 and 0.3 wt %). This change in $E_{\sigma\sigma}$ appears to be a distinctive feature of a transition in the underlying instability mechanism (Steinberg 2022).

Figure 4 shows instantaneous visualizations of the unsteady flow after the onset of instability in a 40 mm 2° cone geometry, and the corresponding space–time diagrams (kymographs) depict the evolution of the unsteady flow with time. The instability originates at the edge of the conical fixture and spirals towards the centre (as can be seen from the fine dark streak spiralling inwards). As the perturbations propagate towards the centre of the cone, they dissipate, which can be clearly seen in the kymographs; the

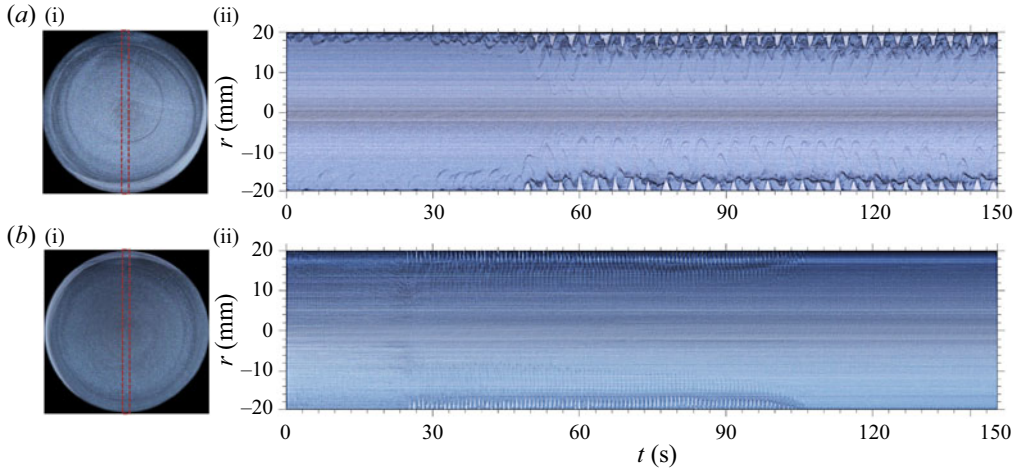

Figure 4. Snapshot of the unsteady torsional flow between a cone and plate with a diameter of 40 mm and 2° cone angle visualized from below. (*a*-i) 3 wt. % PIB solution rotating at $\Omega = 3.5$ rad s^{-1}($Re = 1.15$, $Wi = 31.02$). (*b*-i) 1 wt.% PIB solution at $\Omega = 15$ rad s($Re = 39.8$, $Wi = 16.41$). The instability starts at the outer rim and propagates radially inwards. (*a*-ii) Kymograph showing the temporal evolution of the flow along the rectangular strip marked by the dashed lines in panel (*a*-i). (*b*-ii) Kymograph showing the time evolution of the flow in the rectangular region marked by the dashed lines in panel (*b*-i). The amplitude and the radial extent of the perturbations in the lower concentrated polymer solutions decrease with increasing fluid inertia.

undulating fluctuations are most intense near the edge but become dimmer towards the centre of the cone. The progressive ejection of material from the gap due to time-dependent fluctuations is evident at long times.

3.2. *Hysteresis and determination of critical conditions for onset of instability*

Hysteresis has been observed for Boger fluids in the past following a sudden jump down in shear rate from a value larger than the critical value (after the induction of a time-dependent flow state) to a shear rate lower than the critical value that had initially been determined in a step ramp-up protocol resulting in the onset of time-dependent flow (McKinley *et al.* 1991). These observations are consistent with a subcritical Hopf bifurcation; however, directly accessing the hysteretic state and assessing its extent is easier if the control variable is switched to be the imposed stress. In the present work, we perform both controlled stress sweeps as well as stepped ramps up in imposed shear rate measurements.

The critical values we report for the onset of instability, i.e. $\dot{\gamma}_c$, are determined by loading a fresh fluid sample and then performing a series of step increases in the shear rate. At each new shear rate, the evolution in the shear stress and the normal stress difference is followed for a long time (≈30 min) to observe the possible onset of a time-dependent unstable flow at a constant applied shear rate (see figure 3*a*). The lowest shear rate at which such a transition was observed is then determined to be the critical shear rate. These critical values are indicated by the arrows in figure 5. We call this a 'stepped shear rate ramp-up' protocol. However, the transition might be hysteretic in the sense that if one has to 'step down' from an unstable flow rate, the flow might only become stable at a shear rate lower than the critical value obtained in a 'stepped ramp-up' experiment. To explore the presence and extent of flow hysteresis, we perform a continuous slow ramp-up and subsequent ramp-down in the shear stress (i.e. a saw-tooth stress profile) using the same

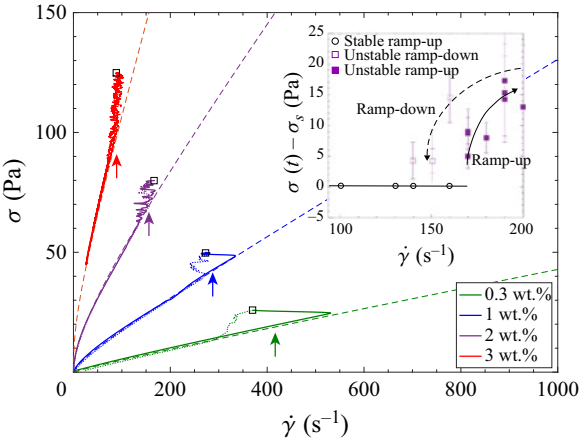

Figure 5. Stress versus shear-rate data for the various PIB solutions used in this study for a continuous stress ramp-up experiment in a 40 mm 2° cone-and-plate geometry. In the continuous stress ramp-up experiment, fluids were subjected to a linearly increasing stress given by $\sigma(t) = \sigma_0(1 + t/5\tau_s)$ (solid lines) up to a maximum stress (indicated by hollow black square symbols for each fluid) in the unstable time-dependent flow region. The stress was then reduced linearly from its maximum value (dotted lines) at the same rate as the ramp-up, and the instability was monitored by observing the resulting shear rate $\dot{\gamma}(t)$. Hysteresis in the critical shear rate can be inferred from whether the curve returns to its base state (shown by dashed lines, which is the Cross model fitted to the steady-flow curve data) or not. We observe that all the fluids undergo a hysteretic transition to an unsteady time-fluctuating state. The critical shear rate values measured from the stepped-up stress growth protocol are also shown as vertical arrows. The inset shows a hysteretic bifurcation curve in stepped shear rate ramp-up and ramp-down experiments for the 2 wt.% fluid.

geometry on a stress-controlled rheometer. In this protocol, we continuously increase the shear stress imposed on the sample (linearly in time) until the flow becomes unstable, and then slowly and continuously reduce the applied stress. By 'slow', we mean that the rate of increasing the applied stress is much slower than the stress relaxation time for the fluids; here, we use a ramp rate of $1/5\tau_s$. In the absence of flow instability, such a protocol should trace out the steady flow curve predicted by the fit of the Cross model for each fluid (shown by the dashed lines in figure 5). Hysteresis in the apparent flow curve of shear stress versus shear rate can thus be directly confirmed by departures from this flow curve, as shown in figure 5.

It is evident from figure 5 that the presence of strong viscoelastic shear-thinning reduces the magnitude of the flow hysteresis observed in the purely elastic case (for the 2 wt.%, 3 wt.% fluids); however, careful measurements using the stepped shear rate ramp-up and ramp-down protocols, and subtraction of the steady state flow stress σ_s, reveal that a small amount of hysteresis is still present (e.g. see the inset of figure 5 for the 2 wt.% fluid). In the case of the inertio-elastic instability observed for the 0.3 and 1 wt.% fluids, it is clear that the extent of flow hysteresis is very pronounced (with $\Delta\dot{\gamma}_c = \dot{\gamma}_c^{up} - \dot{\gamma}_c^{down} \approx 100\ \text{s}^{-1}$).

3.3. *Mapping the instability transition in the Wi–Re plane*

The changes in the magnitude of the stress fluctuations and the power law slope of the power spectra suggest a transition in the underlying mechanism behind the onset of instability as we change the polymer concentration. Experiments with a range of cone-and-plate geometries ranging from $\{R, \theta\} = \{2\ \text{cm}, 1°\}$ to $\{1.25\ \text{cm}, 5°\}$ also show that the critical conditions vary systematically with changes in the geometric parameter

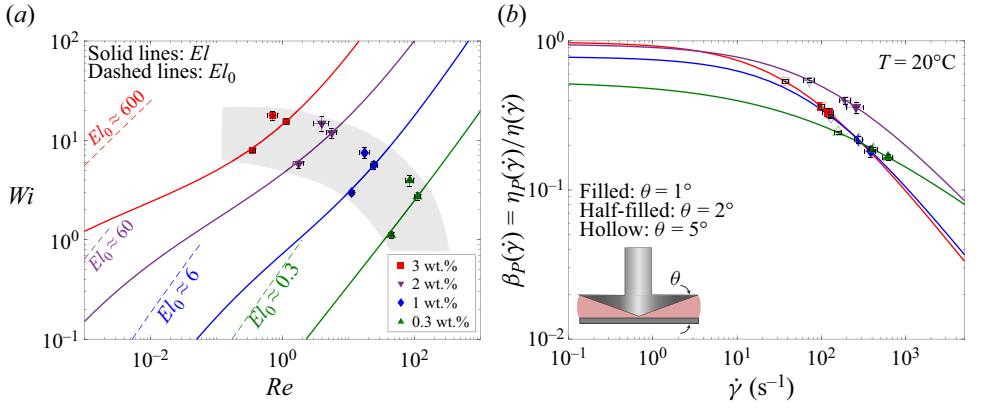

Figure 6. (*a*) Critical state diagram for the onset of complex instability for three different geometries and four fluid compositions projected onto the *Wi*–*Re* plane. The samples tested span approximately four orders of magnitudes in elasticity number, and the instability mechanism shifts from purely elastic to elasto-inertial as we reduce the polymer concentration. Shear thinning shifts the onset of instability to a higher Re_c at a fixed *Wi*, as demonstrated by the two different curves representing the elasticity numbers defined by $El = Wi/Re$. The solid curve $El = Wi/Re$ incorporates the shear-thinning effect. The dashed lines are the zero shear-rate elasticity number $El_0 = Wi_0/Re_0$ without considering shear thinning. (*b*) Shear-thinning parameter $\beta_P(\dot{\gamma})$ as a function of the shear rate and the critical shear rates for the onset of time-dependent flows for the different PIB solutions in different geometries. Symbols are experimentally determined critical values of $\dot{\gamma}$ and the associated flow parameters Wi_c and Re_c.

$1/\theta$. These changes can be understood more quantitatively by projecting the critical conditions for the onset of instability onto the *Wi*–*Re* plane (Datta *et al.* 2022) as illustrated in figure 6(*a*). The transition from purely elastic to elasto-inertial can be clearly demonstrated by considering the evolution in the elasticity number $El = Wi/Re$ with shear-thinning effects (solid lines). The elasticity number quantifies the relative magnitude of viscoelastic and inertial effects in the *Wi*–*Re* state diagram. The trajectory followed by highly elastic fluids with a constant viscosity η_0 (i.e. Boger fluids) is represented in figure 6(*a*) by dashed lines with constant slopes ($El_0 = Wi_0/Re_0$). By including the effect of shear thinning through the rate-dependent viscosity of the PIB solutions, we can conclude that shear thinning shifts the critical Reynolds number Re_c for the onset of instability to a substantially higher value (at a given Weissenberg number). The value of the elasticity number at the onset of instability El_c reduces by four orders of magnitude (from ≈800 to 0.02) as we reduce the concentration of the PIB solution by one order of magnitude (from 3 wt.% to 0.3 wt.%), signifying the rapid rise in inertial effects compared with viscoelastic effects.

At low *Re*, shear thinning increases the stability of the torsional shear flow of viscoelastic fluids against the onset of purely elastic instabilities. For example, the Boger fluid used by Schiamberg *et al.* (2006) exhibited purely elastic instability beyond $Wi_c \approx O(1)$ compared with the values of $Wi_c \sim O(10)$ required for an elastic but strongly shear-thinning PIB solution. However, reducing the concentration of the PIB solutions also decreases the extent of shear thinning, i.e. the magnitude of changes in β_P are reduced, and the onset of instability shifts to $Wi_c \sim O(1)$. Thus, reducing the extent of shear-thinning (or maintaining β_P closer to unity) drives the earlier onset of elastic instability when represented in terms of *De* or *Wi*.

The gradual increase in inertial effects is another crucial factor contributing to shifts in the onset conditions of the instability with a reduction in the PIB concentration. It is

observed that the presence of elasticity makes the flow unstable at much lower Reynolds numbers ($Re_c \lessapprox 100$) compared with the critical value of $\rho\Omega_c R^2/\eta$ required for the onset of purely inertial turbulence in cone–plate flows of Newtonian fluids. Finally, the shaded region, which is included solely as a guide for the eye, hints at common trends and the possible collapse of all the critical conditions onto a single master curve. In the following section, we seek a unified critical condition spanning purely elastic to elasto-inertial regimes for a range of polymer concentrations and flow geometries.

3.4. *Bridging elasticity and inertia: a unified instability criterion for the onset of instability in torsional flows of shear-thinning viscoelastic fluids*

The governing role of shear thinning in stabilizing the flow of the PIB solutions can be seen from the magnitudes of the decrease in $\beta_P(\dot{\gamma})$ shown in figure 6(*b*) with shear rate and/or decreasing PIB concentration. In addition, (2.3) shows that the shear relaxation time is also a shear-thinning function of the shear rate and this plays an important role in determining the onset of instability. These nonlinear effects of shear thinning can be incorporated heuristically in the critical conditions for the onset of a purely elastic instability by incorporating the rate-dependence of the relaxation time $\tau_s(\dot{\gamma})$ from (2.3) into (1.2):

$$\frac{\tau_s U}{\mathcal{R}}\frac{N_1}{\sigma} \equiv \frac{\tau_s(\dot{\gamma})U}{\mathcal{R}}\frac{N_1}{\sigma} = \frac{U}{\mathcal{R}}\frac{2}{\beta_P(\dot{\gamma})\dot{\gamma}}\left(\frac{N_1}{2\sigma}\right)^2 \geq M_c^2. \tag{3.1}$$

In a cone and plate geometry with cone angle θ and radius $\mathcal{R} = R$ rotating with a rate Ω, we get the characteristic velocity $U = \Omega R$ and shear rate $\dot{\gamma} = \Omega/\theta$. Using these characteristic values and the general definition of the Weissenberg number $Wi = N_1/2\sigma$, a further simplification of (3.1) can be obtained for a cone-and-plate geometry:

$$\frac{2\theta}{\beta_P(\dot{\gamma})}\left(\frac{N_1}{2\sigma}\right)^2 = \frac{2\theta}{\beta_P(\dot{\gamma})}Wi^2 \geq M_c^2. \tag{3.2}$$

Thus, (3.2) gives a critical condition for the onset of purely elastic instability incorporating the effects of shear thinning, viscoelasticity and changes in flow geometry. We note that the critical condition of (1.2) for the onset of purely elastic instabilities in constant viscosity Boger fluids (McKinley *et al.* 1996) can be recovered from (3.2) by substituting the well-known Oldroyd-B results for $N_1 = 2\eta_P\tau_s\dot{\gamma}^2$ and $\sigma = \eta_0\dot{\gamma}$. Curves of neutral stability consistent with (3.2) can also be drawn in the $Wi - \beta_P(\dot{\gamma})/\theta$ plane, where the effects of shear thinning can be incorporated by shifting the geometric parameter $1/\theta$ by an amount depending on the shear-thinning parameter $\beta_P(\dot{\gamma})$ (Öztekin *et al.* 1994). These curves of neutral stability (dotted lines) incorporating shear-thinning and geometry effects in the purely elastic critical instability criterion along with the experimentally measured critical conditions are presented in figure 7(*a*) using the values of $\beta_P(\dot{\gamma}_c)$ shown in figure 6(*b*). We can immediately conclude that the critical conditions shown in figure 6(*a*) would only be shifted vertically by this scaling. This modified critical stability condition still does not incorporate the effects of fluid inertia.

A unified critical condition must ultimately be deduced by performing a rigorous linear stability analysis of the elasto-inertial flow problem. In the absence of any such existing analysis, our empirical measurements can be harnessed to guide the formulation of a unified critical condition. Purely elastic instability arises due to nonlinearities in the fluid constitutive equations, while purely inertial Newtonian turbulence arises from the nonlinearities in the advective term of the equation of motion. The distinct origins

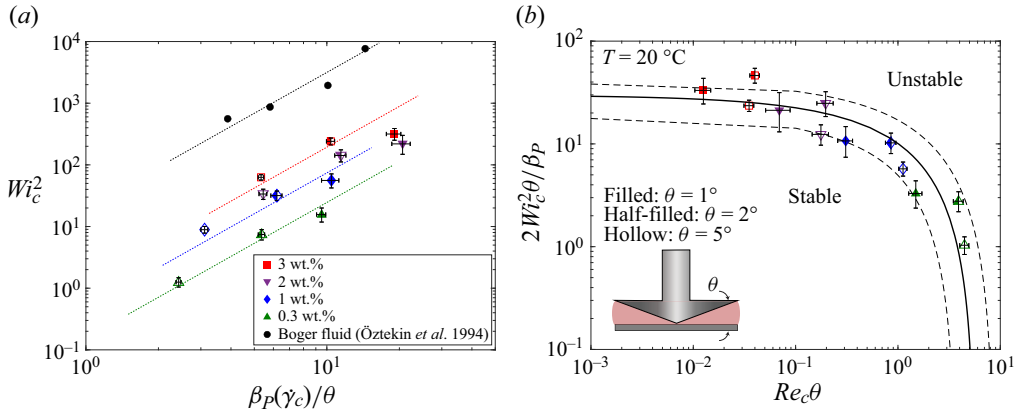

Figure 7. (*a*) Predictions of the augmented purely elastic instability criterion incorporating the effects of shear thinning in fluid rheology (3.2) using the values of $\beta_P(\dot{\gamma}_c)$ shown in figure 6(*b*) for four different fluids used in four different geometries. Boger fluid results are also presented for comparison. It can be concluded that the data lie on different stability curves (dotted lines to guide the eye), which are shifted due to the presence of inertia. Hence, a single elasto-inertial stability curve should incorporate inertial effects. (*b*) Updated state diagram obtained by scaling the axes to incorporate the effects of fluid elasticity, inertia, shear thinning and geometry using (3.6). This state diagram describes the onset of elasticity over a wide range of *Re* and *Wi* spanning four decades in the elasticity number *El* and four different shear-thinning viscoelastic fluids. Dashed lines show 68 % confidence interval corresponding to one standard deviation interval.

of the two sources of nonlinearity suggest that from the viewpoint of infinitesimal perturbations, the two destabilizing terms may be coupled together so that instability ensues when some combination of elastic effects and inertial effects becomes larger than a threshold or a critical value.

The effects of nonlinear elasticity and shear thinning on the steady base torsional shearing flows are already included in (3.1); this *purely elastic* criterion just needs to be augmented by the appropriate nonlinear term to incorporate the effects of fluid inertia in determining the onset of instability. In addition, this unified criterion should: (1) recover the critical instability condition for the onset of purely elastic instability in the absence of inertia; (2) recover the critical instability condition for the onset of purely inertial instability in the absence of elasticity; and (3) predict a smooth transition between the two asymptotic regimes, as observed in figure 6(*a*).

Detailed linear stability analyses (Joo & Shaqfeh 1994; Öztekin *et al.* 1994) consider infinitesimal perturbations to the base flow velocity and stress variables $(\boldsymbol{v}^0, \boldsymbol{\sigma}^0)$ as well as the corresponding velocity and stress gradients $(\boldsymbol{\nabla v}^0, \boldsymbol{\nabla \sigma}^0)$ present in the specific flow field of interest. In the inertialess limit, the perturbed velocity and stress fields can be written in the dimensionless form $\boldsymbol{v} = \boldsymbol{v}^0 + Wi\boldsymbol{v}' + O(Wi^2)$ and $\boldsymbol{\sigma} = \boldsymbol{\sigma}^0 + Wi\boldsymbol{\sigma}' + O(Wi^2)$ (where the stress tensor has been non-dimensionalized with the characteristic viscous stress $\sim \eta_0 U/\mathcal{R}$). Substituting these forms into the governing equations and collecting terms at the first order results in a complex eigenvalue problem involving terms of the form $Wi(\boldsymbol{\nabla v}^0 \cdot \boldsymbol{\sigma}')$, $Wi(\boldsymbol{v}^0 \cdot \boldsymbol{\nabla \sigma}')$, etc. (see Joo & Shaqfeh 1994, Shaqfeh 1996 for details). From a scaling viewpoint, the resulting stability criterion is always in the form of (1.1), or equivalently,

$$\sqrt{\tau_s \frac{U}{\mathcal{R}} \frac{N_1}{\sigma}} \geq M_c. \tag{3.3}$$

Similarly, for the onset of Newtonian curved streamline instabilities, the perturbations can be written in the form $\boldsymbol{v} = \boldsymbol{v}^0 + Re\boldsymbol{v}' + O(Re^2)$ and the eigenvalue problem arises from coupling between the advective terms of the form $Re\boldsymbol{v}^0 \cdot \boldsymbol{\nabla v}'$, $Re\boldsymbol{v}' \cdot \boldsymbol{\nabla v}^0$, etc. From a scaling viewpoint, the resulting relevant dimensionless group that arises is the Görtler number $G = Re(\delta/\mathcal{R})^{3/2}$ (Saric 1994), which couples streamline curvature parametrized by a characteristic radius of curvature $\mathcal{R}$, inertial effects parametrized by a Reynolds number and a small parameter $\epsilon = \delta/\mathcal{R}$ parametrized by the ratio of boundary layer thickness δ to the radius of curvature $\mathcal{R}$. In a Taylor–Couette flow, however, the relevant dimensionless group that arises is the Taylor number $Ta = Re^2\epsilon^3$, which also couples inertial effects parametrized by Reynolds number and a small parameter $\epsilon = h/\mathcal{R}$, where h is the gap between two concentric cylinders. The dimensionless grouping on the left-hand side of (3.3) can be viewed as a viscoelastic Görtler number (Pakdel & McKinley 1996). These arguments all suggest that inertial effects can be parametrized by combining the Reynolds number and a flow geometry-dependent small parameter. So, to quantify inertial nonlinearities, we use the dimensionless ratio of the dynamic pressure ρU^2 compared with the shear stress σ, i.e.

$$\frac{\rho U^2}{\sigma} \geq C^2 \text{ or equivalently } \sqrt{\frac{\rho U^2}{\sigma}} \geq C, \tag{3.4}$$

where C is some critical value of this ratio. We note that this ratio is of the same functional form as the dimensionless stress ratio N_1/σ, which determines the purely elastic instability. Furthermore, as Renardy (2000) has noted in strongly nonlinear elastic flows streamline tension (which scales with N_1), gives rise to a modified form of the inviscid Euler or Bernoulli equation. This scaling in (3.4) automatically gives rise to a combination of Reynolds number and a small parameter to quantify the inertial effects, similar to Görtler and Taylor numbers, as will be evident in the discussion below.

A full inertioelastic linear stability analysis must, ultimately, consider perturbations arising from both elastic effects and inertial effects as well as cross-coupling terms that scale as $ReWi\boldsymbol{v}'$. The resulting eigenvalue problem will be extremely complex, but from a dimensional viewpoint, it must embody the two limits, purely elastic and purely inertial, discussed above, as well as relevant cross-terms. The simplest possible functional form that captures these limits as well as cross-coupling between the elastic stresses and inertial perturbations is a linear combination of the two dimensionless groupings in (3.3) and (3.4). This linear combination can be written in the generic form

$$\sqrt{\frac{\tau_s U}{\mathcal{R}}\frac{N_1}{\sigma}} + \alpha\sqrt{\frac{\rho U^2}{\sigma}} \geq \tilde{M}_c \text{ or equivalently } \left[\sqrt{\frac{\tau_s U}{\mathcal{R}}\frac{N_1}{\sigma}} + \alpha\sqrt{\frac{\rho U^2}{\sigma}}\right]^2 \geq \tilde{M}_c^2, \tag{3.5}$$

where α is a dimensionless weighting parameter and $\tilde{M}_c$ is the critical disturbance magnitude (as modified by the inertial effects). Expanding the square in the second equality gives the locus of the critical conditions. Further simplification of (3.5) in a cone-and-plate geometry can be obtained by using (3.2) and substituting the characteristic velocity $U = \Omega R$ and $\dot{\gamma} = \Omega/\theta$ so that at the critical condition $\dot{\gamma} \to \dot{\gamma}_c$, we require

$$\sqrt{\frac{2\theta}{\beta_P(\dot{\gamma})}Wi^2} + \alpha\sqrt{Re\theta} \geq \tilde{M}_c \text{ or equivalently } \quad \theta\left[\sqrt{\frac{2Wi^2}{\beta_P(\dot{\gamma})}} + \alpha\sqrt{Re}\right]^2 \geq M_c^2, \tag{3.6}$$

where a rate-dependent Reynolds number $Re = \rho\Omega R^2/\eta(\dot{\gamma})$ and also the (small) geometry parameter θ appears naturally in the inertial term. This new generalized criterion in (3.6) asymptotically recovers the purely elastic instability condition ((3.2)) when inertia is negligible, i.e. $Re \to 0$, and also predicts the onset of secondary motion due to inertial effects in Newtonian fluids in a cone-and-plate geometry when the product $Re\theta$ exceeds a critical value consistent with earlier perturbation analyses and experiments (Fewell & Hellums 1977; Sdougos *et al.* 1984).

In lieu of formal linear stability analysis, this unified critical condition can be validated empirically with experimental measurements. We use the result from (2.1), which indicates that N_1 varies quadratically with σ to calculate the critical Weissenberg number $Wi_c = A\sigma(\dot{\gamma}_c)/2$ with $A = 0.29$ obtained from the regression of the experimental measurements presented in figure 2. If the condition suggested by (3.6) is true, then plotting data for the onset of instability in the $Wi^2\theta/\beta_P(\dot{\gamma})$ versus $Re\theta$ phase space should lie on a single curve. We find that this is indeed true for a suitable value of the dimensionless weighting parameter $\alpha = 2.29$ obtained using a two-parameter best fit of the experimental data to the first expression in (3.6) and the result is shown by the solid line figure 7(*b*). The collapse of the data over three orders of magnitude in the elasticity number for four different viscoelastic fluids with varying shear-thinning strengths and for three different conical geometries strongly corroborates the functional form of the unified critical condition for the elasto-inertial instability given in (3.6). The least square curve fitting of (3.6) to experimental measurements of the critical conditions gives $\tilde{M}_c \approx 5.46$.

A further check of the unified critical condition (3.6) can be performed by checking if $\tilde{M}_c \approx 5.46$ obtained from our experimental measurements is consistent with critical conditions in the limiting cases of purely elastic instability of a Boger fluid and a purely inertial instability of a Newtonian fluid in a cone-and-plate geometry. We therefore project the dimensionless criterion represented by (3.6) (with $\alpha \simeq 2.29$ and $\tilde{M}_c \simeq 5.46$) in the modified *Wi*–*Re* plane to incorporate the effects of shear thinning and flow geometry as shown in figure 7(*b*). Our heuristic blending rule provides a good collapse of all the experimental data shown in figure 6(*a*). A typical non-shear-thinning Boger fluid has $\beta_P(\dot{\gamma}) \equiv \beta \simeq 0.4$ and $Re \to 0$, which recovers $Wi_c \approx 60$ consistent with previous experimental observations (McKinley *et al.* 1991). However, for a Newtonian fluid, (3.6) predicts the onset of the unsteady secondary flow in a cone-and-plate geometry at $Re\theta \lesssim 5.68$, which is consistent with, but smaller than, the value deduced from early visualization experiments of Sdougos *et al.* (1984). This scaling form can, in principle, be readily extended to other geometries by the appropriate determination of the radius of curvature of the streamlines, the characteristic flow velocity and the identification of the appropriate characteristic shear rate (McKinley *et al.* 1996). For example, in a parallel plate geometry, the small geometric factor would be H/R, where H is the gap height between the plates.

In the spirit of Occam's razor, we have proposed the simplest possible physically reasonable criterion (additively combining the destabilizing effects of elasticity and inertia). We hope that our results will serve as a motivator for a more detailed stability analysis that fully considers the cross-coupling of perturbation terms between the equation of motion and the nonlinear viscoelastic constitutive equation.

4. Conclusions

We have investigated the onset of time-dependent instabilities in the torsional shearing flow between a cone and a plate with $1^\circ \leq \theta \leq 5^\circ$ for a range of viscoelastic shear-thinning fluids. The onset of instability depends on the coupling between the fluid elasticity,

inertia, shear thinning and flow geometry. Specifically, shear thinning in the fluid rheology stabilizes the unidirectional torsional base flow, while inertia destabilizes it. Furthermore, the systematic changes in the critical conditions and the change in the slope of the power spectra $E_{\sigma\sigma}$ suggests a transition in the instability mechanism from purely elastic to elasto-inertial as we reduce the polymer concentration (and the extent of shear thinning). We show how to represent this multidimensional flow instability transition by constructing a state diagram of critical conditions in the *Wi–Re* plane. Finally, we propose a unified criterion (3.5) to predict the onset of elasto-inertial instability by augmenting the existing criterion for purely elastic instability to include shear thinning and coupling to perturbations arising from inertial effects in the Cauchy momentum equation. We validate the form of this unified criterion empirically with our experimental measurements of the critical conditions for a range of viscoelastic fluids and different conical geometries. The data collapse over a wide range of conditions corroborates the final functional form of (3.6) at least for a cone-and-plate geometry. Extending this unified criterion to other torsional flow geometries (like the parallel plate geometry and Taylor–Couette flow) using an appropriate Görtler number would provide further verification of this representation.

Supplementary material. Supplementary material are available at https://doi.org/10.1017/jfm.2024.254.

Acknowledgements. The authors would like to thank Lubrizol Inc. for financial support and for providing the components required to formulate the polymeric fluids used in this study.

Declaration of interests. The authors report no conflict of interest.

Author ORCIDs.
Rishabh V. More https://orcid.org/0000-0003-3922-2519;
G.H. McKinley https://orcid.org/0000-0001-8323-2779.

References

Binding, D., Jones, D. & Walters, K. 1990 The shear and extensional flow properties of M1 fluid. *J. Non-Newtonian Fluid Mech.* **35** (2–3), 121–135.

Bird, R.B., Armstrong, R.C. & Hassager, O. 1987 *Dynamics of Polymeric Liquids. Vol. 1: Fluid Mechanics*. John Wiley and Sons.

Calado, V.M., White, J.M. & Muller, S.J. 2005 Transient behavior of Boger fluids under extended shear flow in a cone-and-plate rheometer. *Rheol. Acta* **44**, 250–261.

Chandra, B., Mangal, R., Das, D. & Shankar, V. 2019 Instability driven by shear thinning & elasticity in the flow of concentrated polymer solutions through microtubes. *Phys. Rev. Fluids* **4** (8), 083301.

Datta, S.S., *et al.* 2022 Perspectives on viscoelastic flow instabilities and elastic turbulence. *Phys. Rev. Fluids* **7** (8), 080701.

Dutcher, C.S. & Muller, S.J. 2009 The effects of drag reducing polymers on flow stability: insights from the Taylor–Couette problem. *Korea-Australia Rheol. J.* **21** (4), 213–223.

Dutcher, C.S. & Muller, S.J. 2013 Effects of moderate elasticity on the stability of co-and counter-rotating Taylor–Couette flows. *J. Rheol. (NY)* **57** (3), 791–812.

Fewell, M.E. & Hellums, J. 1977 The secondary flow of Newtonian fluids in cone-and-plate viscometers. *Trans. Soc. Rheol.* **21** (4), 535–565.

Graessley, W.W. 1980 Polymer chain dimensions and the dependence of viscoelastic properties on concentration, molecular weight and solvent power. *Polymer* **21** (3), 258–262.

Heo, Y. & Larson, R.G. 2005 The scaling of zero-shear viscosities of semidilute polymer solutions with concentration. *J. Rheol. (NY)* **49** (5), 1117–1128.

Jackson, K., Walters, K. & Williams, R. 1984 A rheometrical study of Boger fluids. *J. Non-Newtonian Fluid Mech.* **14**, 173–188.

Joo, Y.L. & Shaqfeh, E.S. 1994 Observations of purely elastic instabilities in the Taylor–Dean flow of a Boger fluid. *J. Fluid Mech.* **262**, 27–73.

KIBBELAAR, H.M., DEBLAIS, A., BRIAND, G., HENDRIX, Y., GAILLARD, A., VELIKOV, K., DENN, M. & BONN, D. 2023 Towards a constitutive relation for emulsions exhibiting a yield stress. *Phys. Rev. Fluids* **8** (12), 123301.

LACASSAGNE, T., CAGNEY, N. & BALABANI, S. 2021 Shear-thinning mediation of elasto-inertial Taylor–Couette flow. *J. Fluid Mech.* **915**, A91.

LARSON, R.G. 1992 Instabilities in viscoelastic flows. *Rheol. Acta* **31** (3), 213–263.

LODGE, A., AL-HADITHI, T. & WALTERS, K. 1987 Measurement of the first normal-stress difference at high shear rates for a polyisobutylene/decalin solution 'D2'. *Rheol. Acta* **26** (6), 516–521.

MCKINLEY, G.H., BYARS, J.A., BROWN, R.A. & ARMSTRONG, R.C. 1991 Observations on the elastic instability in cone-and-plate and parallel-plate flows of a polyisobutylene Boger fluid. *J. Non-Newtonian Fluid Mech.* **40** (2), 201–229.

MCKINLEY, G.H., ÖZTEKIN, A., BYARS, J.A. & BROWN, R.A. 1995 Self-similar spiral instabilities in elastic flows between a cone and a plate. *J. Fluid Mech.* **285**, 123–164.

MCKINLEY, G.H., PAKDEL, P. & ÖZTEKIN, A. 1996 Rheological and geometric scaling of purely elastic flow instabilities. *J. Non-Newtonian Fluid Mech.* **67**, 19–47.

MORE, R.V., PATTERSON, R., PASHKOVSKI, E. & MCKINLEY, G.H. 2023 Rod-climbing rheometry revisited. *Soft Matt.* **19** (22), 4073–4087.

OLAGUNJU, D.O. 1995 Elastic instabilities in cone-and-plate flow: small gap theory. *Z. Angew. Math. Phys.* **46**, 946–959.

OLAGUNJU, D.O. 1997 Hopf bifurcation in creeping cone-and-plate flow of a viscoelastic fluid. *Z. Angew. Math. Phys.* **48** (3), 361–369.

OLAGUNJU, D.O. & COOK, L.P. 1993 Secondary flows in cone and plate flow of an Oldroyd-B fluid. *J. Non-Newtonian Fluid Mech.* **46** (1), 29–47.

ÖZTEKIN, A., BROWN, R.A. & MCKINLEY, G.H. 1994 Quantitative prediction of the viscoelastic instability in cone-and-plate flow of a boger fluid using a multi-mode Giesekus model. *J. Non-Newtonian Fluid Mech.* **54**, 351–377.

PAKDEL, P. & MCKINLEY, G.H. 1996 Elastic instability and curved streamlines. *Phys. Rev. Lett.* **77** (12), 2459.

RENARDY, M. 2000 Current issues in non-Newtonian flows: a mathematical perspective. *J. Non-Newtonian Fluid Mech.* **90** (2–3), 243–259.

SARIC, W.S. 1994 Görtler vortices. *Annu. Rev. Fluid Mech.* **26** (1), 379–409.

SCHAEFER, C., MOROZOV, A. & WAGNER, C. 2018 Geometric scaling of elastic instabilities in the Taylor–Couette geometry: a theoretical, experimental and numerical study. *J. Non-Newtonian Fluid Mech.* **259**, 78–90.

SCHIAMBERG, B.A., SHEREDA, L.T., HU, H. & LARSON, R.G. 2006 Transitional pathway to elastic turbulence in torsional flow of a polymer solution. *J. Fluid Mech.* **554**, 191–216.

SDOUGOS, H.P., BUSSOLARI, S.R. & DEWEY, C.F. 1984 Secondary flow and turbulence in a cone-and-plate device. *J. Fluid Mech.* **138**, 379–404.

SHAQFEH, E.S.G. 1996 Purely elastic instabilities in viscometric flows. *Annu. Rev. Fluid Mech.* **28** (1), 129–185.

STEINBERG, V. 2022 New direction and perspectives in elastic instability and turbulence in various viscoelastic flow geometries without inertia. *Low Temp. Phys.* **48** (6), 492–507.

WHITE, J.L. 1964 Dynamics of viscoelastic fluids, melt fracture, and the rheology of fiber spinning. *J. Appl. Polym. Sci.* **8** (5), 2339–2357.